# Vortex-induced vibration of long flexible cylinder in uniform cross-flow

\* Chunning Ji [1], Ziteng Peng [2], Md. Mahbub Alam [3],
Weilin Chen [4] and Dong Xu [5]

[1), 2), 4), 5)] *State Key Laboratory of Hydraulic Engineering Simulation & Safety, Tianjin University, Tianjin, 300072, China*
[3)] *Institute for Turbulence-Noise-Vibration Interaction and Control, Shenzhen Graduate School, Harbin Institute of Technology, Shenzhen 518055, China*
[1)] *cnji@tju.edu.cn*

## ABSTRACT

Numerical simulations are performed of a long flexible cylinder undergoing vortex-induced vibration at a Reynolds number of 500. The cylinder is pinned at both ends, having an aspect ratio of 100 (cylinder length to cylinder diameter) and a mass ratio of 4.2 (structural mass to displaced fluid mass). Temporal and spatial information on the cross-flow (CF) and in-line (IL) vibrations is extracted. High modal vibrations up to the $6^{th}$ in the CF direction and the $11^{th}$ in the IL direction are observed. Both the CF and IL vibrations feature a multi-mode mixed pattern. Mode competition is observed. The $2^{nd}$ mode with a low frequency dominates the IL vibration and its existence is attributed to a wave group propagating back and forth along the span. Distributions of fluid force coefficients are correlated to those of the CF and IL vibrations along the span. Histograms of the *x-y* motion phase difference are evaluated from a complete vibration cycle representing the standing or travelling wave pattern. Correlations between the phase difference and the vibrations are discussed. Vortex structures behind the cylinder show an interwoven near-wake pattern when the standing wave pattern dominates, but an oblique near-wake pattern when the travelling wave pattern prevails.

## 1. INTRODUCTION

Vortex-induced vibration (VIV) of slender marine structures is of practical interest to ocean engineering in the actual application. For example, VIV-induced fatigue damage is one of the most common failures for flexible cylindrical marine structures,

---

[1)] Professor
[2)] Graduate Student
[3)] Professor
[4)] Graduate Student
[5)] Associate Professor

such as risers, pipelines and tendons. Recently, great strides have been achieved in understanding the mechanisms involved in this complicated dynamic process and a comprehensive review can be found in Wu et al. (2012).

Previous investigations on VIV of a flexible cylinder are mainly carried out in laboratory water flume and towing tank. Vandiver (1993) experimentally studied the VIV of a flexible cylinder in uniform cross-flow. An empirical formula was proposed to predict the drag force by using the transverse vibration amplitude of the cylinder. Brika and Laneville (1993) investigated the VIV of a flexible cable. The first mode of vibration was excited. It was also found that different vortex-shedding patterns occur at 'lock-in', similar to those observed behind rigid cylinders (Williamson and Roshko, 1988). The switch between the vibration braches shows hysteresis, corresponding to the phase jump between the displacement and the lift. Huera-Huarte and Bearman (2009a, 2009b) carried out a series of laboratory experiments in which a flexible cylinder was partly submerged in water. Three different tensions were adopted. The initial, upper and lower branches were observed in the smallest tension case. Whereas, in the other two cases, the lower branch vanished. It was also found that the dual resonance, i.e. the in-line (IL) and cross-flow (CF) vibrations resonate simultaneously, was featured by the 'figure-eight' trajectories, the third harmonic in lift, and the steady IL to CF vibration phase difference. The 2S vortex-shedding pattern, i.e. two single vortices alternately shed in one cycle, was found near the supporting ends. While the vortex-shedding pattern in the mid-span of the cylinder switched between 2S and 2P (two vortex pairs alternately shed in one cycle). Similar findings were also reported in Chaplin et al. (2005).

Due to the very demanding computational requirements of three-dimensional (3D) computational fluid dynamics (CFD) simulations, the numerical investigation on the VIV of a slender cylinder is rare, especially the one with a large aspect ratio. Newman and Karniadakis (1997) carried out a direct numerical simulation (DNS) of a flexible cylinder in uniform cross-flow. Periodic boundary conditions were applied to simulate the VIV of a slender cylinder with an infinite length. Two vibration modes, i.e. the standing and travelling wave modes, were found. Because of the low-energy feature of the travelling wave mode, the standing wave vibration finally transformed into the travelling wave one. It was also reported in Newman and Karniadakis (1997) that the near-wake showed an oblique vortex-shedding pattern in the travelling wave vibration, but exhibited an interwoven vortex-shedding pattern in the standing wave vibration. Bourguet et al. (2011) numerically investigated the VIV of a flexible cylinder in shear-flow. A combined standing and travelling wave pattern was observed. Lucor et al. (2006) studied the distribution and variation of the hydrodynamic forces on a flexible cylinder undergoing VIV in shear-flow. The influences of different flow profiles, i.e. linear and exponential shear flows, were investigated.

In this paper, the VIV of a flexible cylinder in uniform cross-flow is numerically investigated. The aspect ratio of the cylinder is 100, the Reynolds number is 500, the mass ratio is 4.2, and the normalized tension is 170. The structural damping is set to zero on the purpose of exciting large-amplitude vibrations.

## 2. NUMERICAL METHODOLOGY

The governing equations for fluid flow are the incompressible Navier–Stokes equations. The two-step predictor-corrector procedure is adopted for the decoupling of the flow governing equations. The resultant pressure Poisson equation is solved by using the BiCGSTAB scheme and the conjugated gradient method preconditioned by using the geometric multi-grid method. The second-order Adams-Bashforth time marching scheme is employed to calculate a new velocity field.

The fluid-structure interaction (FSI) is simulated by using the immersed boundary (IB) method which was first introduced by Peskin (1972) in the simulation of blood flow around the flexible leaflet of a human heart. In the framework of the IB method, the flow governing equations are discretized on a fixed Cartesian grid, which generally does not conform to the geometry of moving structures. As a result, the boundary conditions on the fluid-structure interface (which manifest the interaction between fluid and structure) cannot be imposed directly. Instead, an extra body force is added into the momentum equation by using interpolation and distribution functions to take such interaction into account. Compared with conventional FSI numerical methods, the IB method has significant advantages, particularly in the FSI simulations with topological changes. For the sake of conciseness, details of the methodology are not presented here and readers can refer to our previous work (Ji *et al.*, 2012) for further information.

The flexible cylinder is modelled as a pined-pined top tension cable on the consideration of the large aspect ratio of a marine riser in reality. The bending stiffness of the cylinder is neglected. The mass ratio is $m = \rho_c / \rho_f D^2$, where $\rho_c$ is the cylinder mass per unit length, $\rho_f$ is the fluid density, and $D$ is the cylinder diameter. The normalized tension is $T = \tau / \rho_f D^2 U_\infty^2$, where $\tau$ is the tension invariant along the span, and $U_\infty$ is the free-stream velocity. The non-dimensional phase velocity is calculated as $\omega = \sqrt{T/m}$. The non-dimensional i[th] natural frequency in vacuum is $f_{i,v} = \omega / \lambda_i$, where $\lambda_i$ is the normalized i[th] wavelength. The non-dimensional governing equation for the structural dynamic can be expressed as follows.

$$m\ddot{\zeta}(x,y) - T\zeta''(x,y) = \frac{C(x,y)}{2} \tag{1}$$

where, $\zeta(x,y)$ is the displacement normalized by the cylinder diameter, $C(x,y) = 2F(x,y) / \rho_f DU_\infty^2$ is the hydrodynamic force coefficient, $F(x,y)$ is the hydrodynamic force. The superscripts ·· and ″ represent the second-order time and space derivatives, respectively. The governing equation is discretized by using the 3D 2-node cable element. Each node has three degree-of-element (DOF). The Newmark-$\beta$ method which is unconditional stable and second-order accurate is adopted for time marching.
The numerical methodology and the corresponding computing code have been systematically validated and verified in many different simulations, ranging from 2D simulations of the VIV of a single/multiple cylinder(s) in laminar flows to 3D simulations

of the VIV of an isolated cylinder in uniform/shear flows. High accuracy and good fidelity of the numerical results have been proved. Refer to our published papers (Chen *et al.* 2015a, 2015b) for details.

## 3. RESULTS AND DISCUSSIONS

### *3.1 Simulation parameters*

The simulation is carried out in a rectangular computational box $\Omega = [-8D, 32D] \times [-10D, 10D] \times [0, 100D]$ discretized by a Cartesian mesh with a resolution of $512 \times 192 \times 384$ (streamwise $\times$ transverse $\times$ spanwise). The flexible cylinder is initially placed at the origin of the *x-y* plane. In the vicinity of the cylinder (a square region of $[-2D, 22D] \times [-2D, 2D]$ in the *x-y* plane), a uniform mesh with a grid spacing of $\Delta x = \Delta y = D / 32$ is used. Beyond that, a stretched mesh is adapted on the consideration of keeping the total number of grids within a reasonable range. Along the cylinder span, totally 385 planes are adopted with a grid spacing of $\Delta z \approx 0.26D$. The Dirichlet inflow boundary condition is used together with free-slip side boundary conditions. A Neumann-type boundary condition is adopted at the outflow. The number of IB points for the cylinder is 202 on the *x-y* plane to ensure at least one IB point is allocated in each grid cell. Other simulation parameters are: the Reynolds number Re=500, the non-dimensional tension is *T*=170, the mass ratio *m*=4.2 and the normalized time step size is $\Delta t U / D$ =0.0025.

### *3.2 Vibration response*

Fig. 1 shows the maximum and root-mean-square (r.m.s.) amplitudes of the displacement in the IL and CF directions, respectively. Note that the time-averaged streamwise displacement is deducted in the calculation of the IL amplitudes. Both IL and CF amplitudes are symmetric about the cylinder's midpoint at *z*/*D*=50. The IL max amplitude, $A_{x,\max}$, shows two major peaks on which eleven minor peaks superimposed. While the CF max amplitude, $A_{y,\max}$, demonstrates two major peaks on each side and a flattened and spanwise elongated peak in the middle. Obvious fluctuations can be found on this mid-span peak. The largest $A_{x,\max}$ is 0.48*D* achieved at *z*/*D*=25 and 75. It is comparable to the largest $A_{y,\max}$ of 0.84*D* obtained at *z*/*D*=10 and 90. This is different to the VIV response of an elastically-supported rigid cylinder in which the IL amplitude is one order of magnitude smaller that of the CF counterpart. The flattened CF peak in the mid-span implies the predominant travelling wave pattern in this region. While, the enlarged CF peaks near the ends indicates the prevailing standing wave pattern. Moreover, the peak amplitudes near both ends roughly double the one in the middle, suggesting the perfect refection of the propagating wave. The IL and CF r.m.s. amplitudes show similar patterns discussed above except that the variation is smoother. The amplitudes are approximately symmetric about the midpoint, and have the maximum values of 0.16*D* and 0.38*D* in the IL and CF directions, respectively.
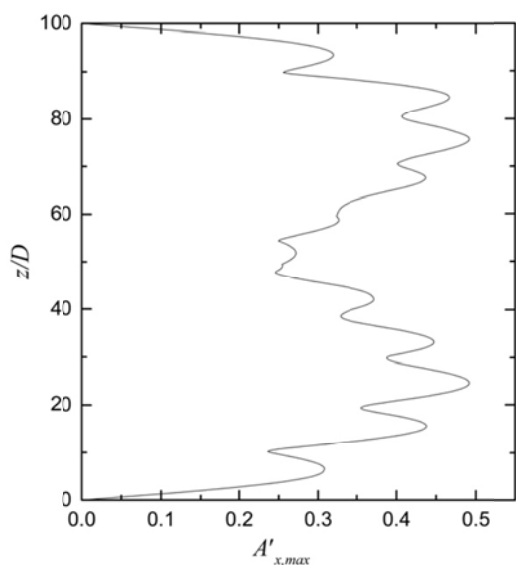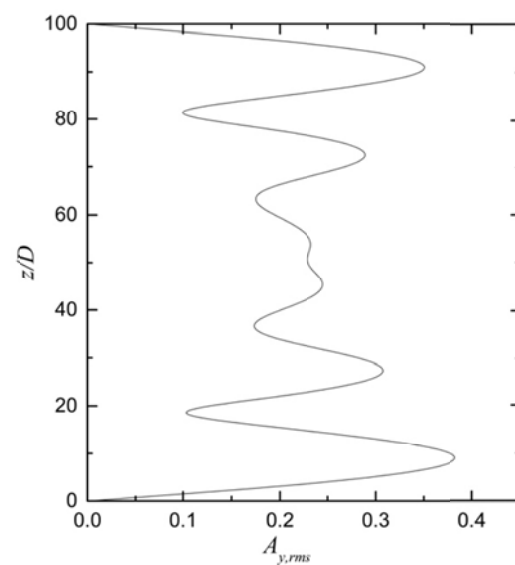
(a) Streamwise maximum amplitude
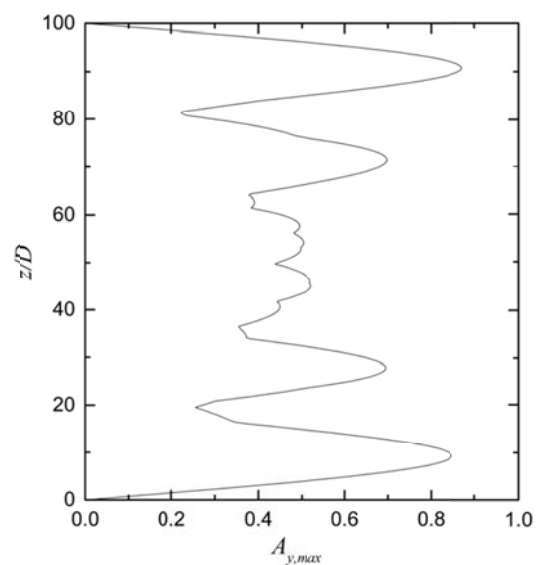
(b) Transverse maximum amplitude
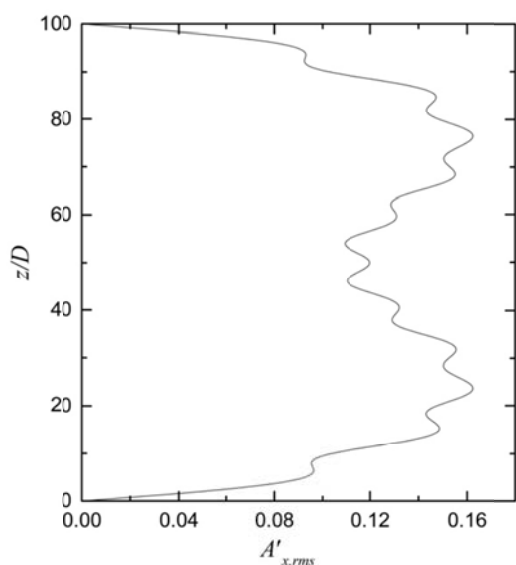
(c) Streamwise root-mean-square
amplitude

(d) Transverse root-mean-square
amplitude

Fig. 1 Distribution of the displacement amplitude along the span.

Fig. 2 shows the time-space distribution of the IL and CF displacement. The combined standing and travelling wave pattern is obvious in the CF displacement. For example, in the mid-span, the CF displacement shows the standing wave pattern during $19.5<tU/D<24$ but displays the travelling wave pattern during $32.5<tU/D<40$. The

two patterns alternately dominate the CF vibration. On the contrary, the IL displacement shows a travelling wave dominated pattern in most of the span. The standing wave pattern is only observed at the very ends due to the wave reflection. The above observations are in consistent with the spanwise distribution of the IL and CF amplitudes, as shown in Fig. 2.

An interesting phenomenon observed is that a wave group composed of several individual waves propagates back and forth along the span. Because the structural damping is zero, the amplitude of the wave group is not significantly reduced, despite of some fluctuations in the IL displacement. When the wave group is reflecting at one end, the displacement shows the standing wave pattern. While, when the wave group is propagating to the other end, the displacement shows the travelling wave pattern.
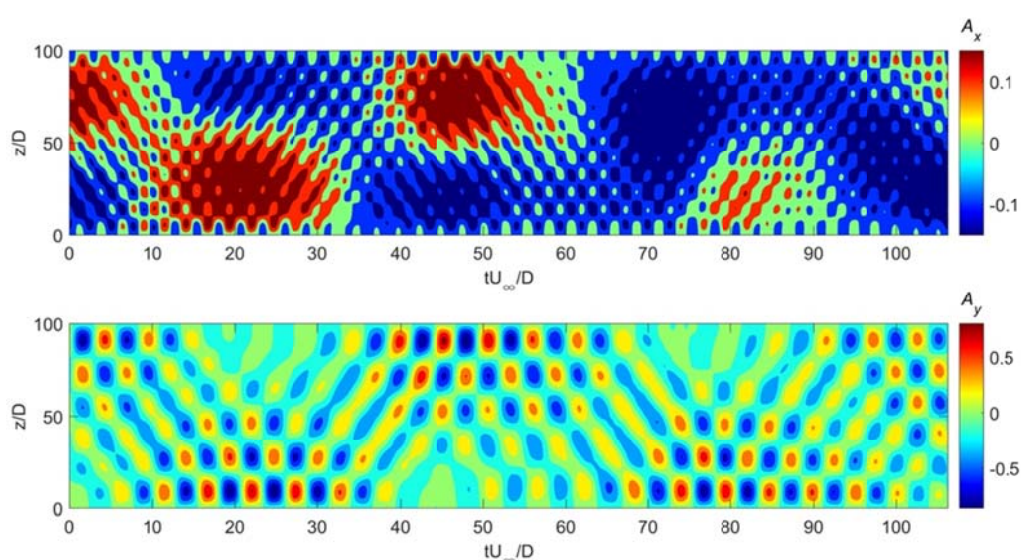


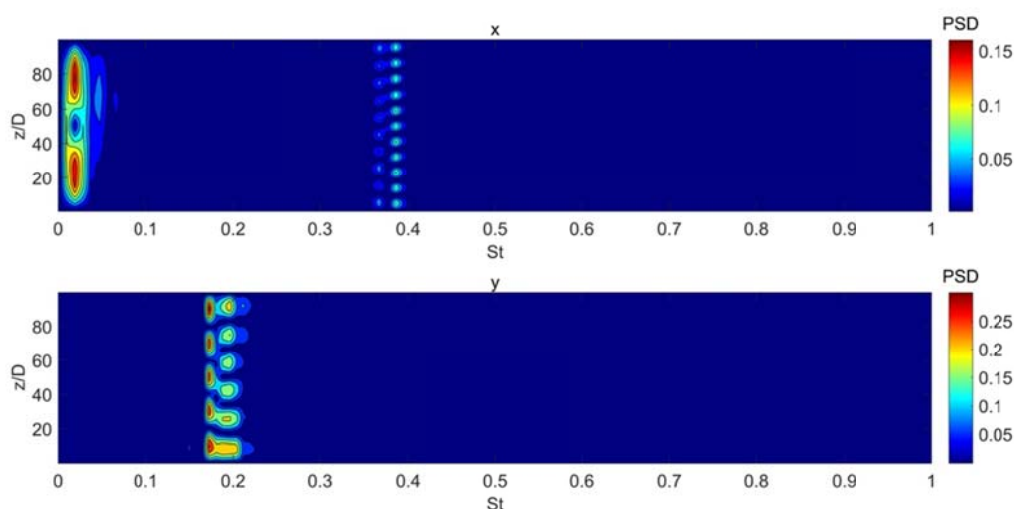Fig. 2 Time-space distribution of the IL (upper) and CF (lower) displacement.



Fig. 3 Power spectral density of the IL and CF displacement.

Fig. 3 shows the distribution of the power spectral density (PSD) of the displacement calculated by using the fast Fourier transform. It can be seen that the IL vibration shows the co-existence of three components, i.e. the 2nd, 10th and 11th mode of vibration. Among these, the 2nd mode is predominant, while the 10th mode is rather weak. The CF vibration consists of the 5th and 6th mode of vibration, with the former slightly prevalent. The multi-mode vibration is the unique feature of the VIV of a flexible cylinder, especially the one with a large aspect ratio. A possible reason is related with the IL bending of the cylinder which gives rise to the varying local normal velocity (and thus the varying local reduced velocity) along the cylinder. However, the 2nd mode of vibration in the IL direction is apparently not related with the IL bending effects but caused by the low-frequency propagating wave group.

The PSD plots of the displacement only show the time-averaged characteristics of the vibration modes. To investigate their temporal evolution, the time histories of the mode of vibration in the IL and CF directions are calculated by applying the mode decomposition method. Obvious mode competition is observed, as shown in Fig. 4. In the IL vibration, the competition is between the 10th and 11th modes. While, in the CF vibration, the competition is between the 5th and 6th modes. Upon closer inspection on the modal histories, it can be found that when the wave group is reflecting at the lower end ($z/D$=0), the CF vibration shows the co-existence of the 5th and 6th modes. However, when the wave group is echoing at the upper end ($z/D$=100), the CF vibration shows a single-mode pattern, either the 5th or 6th mode.
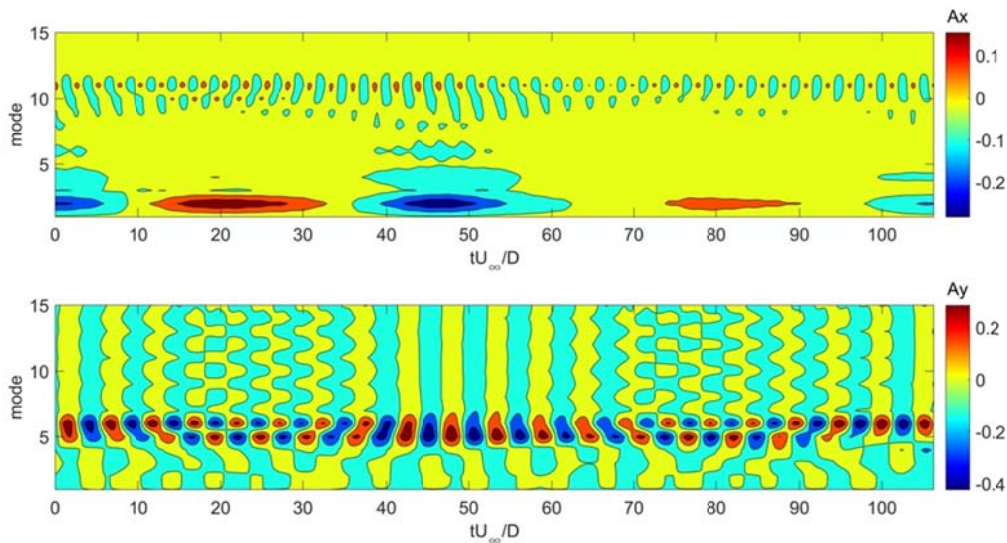


Fig. 4 Time histories of the streamwise and transverse vibration mode.

### 3.3 Hydrodynamic forces

Fig. 5 (a) and (b) show the spanwise distributions of the time-averaged and r.m.s. drag coefficients, $C_{D,avg}$ and $C_{D,rms}$, respectively. It is seen that $C_{D,avg}$ shows six peaks along the span similar to the CF vibration amplitude. However, $C_{D,rms}$ shows a distribution with eleven peaks, which is analogous to the IL vibration amplitude. $C_{D,avg}$ is closely correlated with the time-averaged pressure difference around the cylinder. At

the CF vibration node, the time-averaged pressure behind the cylinder is lower than that at the anti-node due to the larger CF amplitude. This causes the larger $C_{D,avg}$ at the CF vibration node. However, $C_{D,rms}$ is linked with the instantaneous IL vibration and the local vortex-shedding, and thus shows the same variation with that of the IL amplitude. Similarly, the r.m.s. lift coefficient, $C_{L,rms}$, behaviors like the CF vibration amplitude along the span, see Fig. 5(c). In the mid-span, $C_{D,rms}$ is obvious smaller than that near the ends. This can be attributed to the local smaller CF vibration amplitudes.
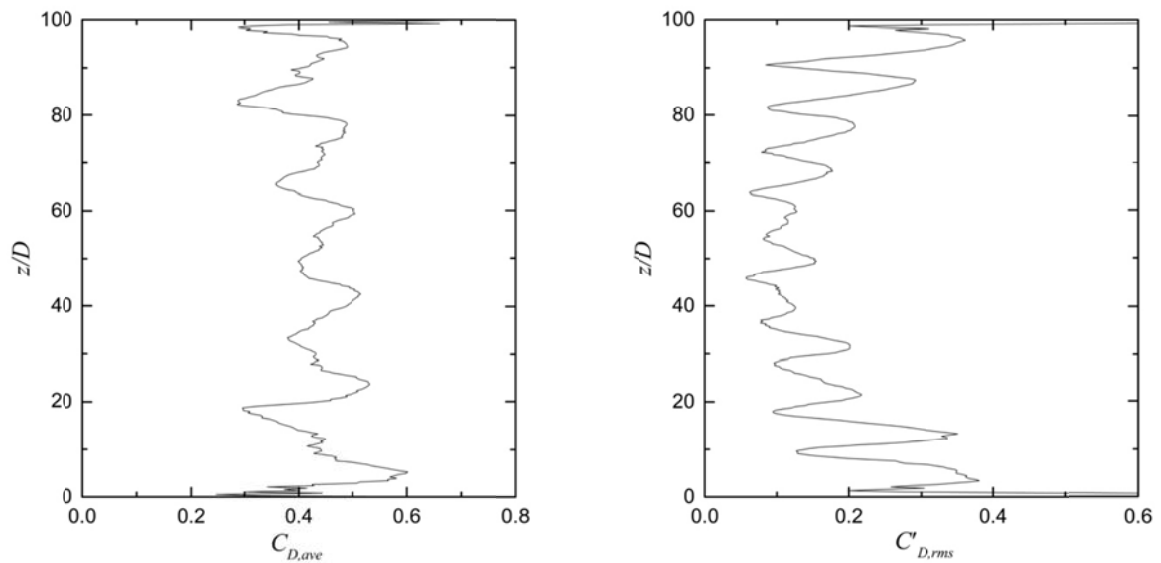


(a) Time-averaged drag coefficient    (b) Root-mean-square drag coefficient
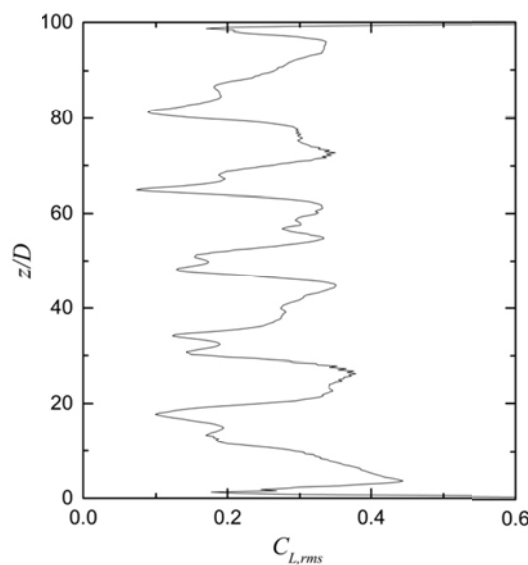


(c) Root-mean-square lift coefficient
Fig. 5 Distribution of the drag and lift coefficients.

### 3.4 Phase difference of x-y motion

According to the suggestion of Bourguet *et al.* (2011), the phase difference between the IL and CF vibrations is defined as

$$\phi_{xy} = [\phi_x - \phi_y, \bmod 360°] \tag{2}$$

where, *p* and *q* are two integer numbers defining the level of synchronization. In this paper, *p* = 1 and *q* = 2 are adopted considering the dominant IL and CF vibration frequencies as shown in Fig. 3. Note that the vibration frequency corresponding to the 2$^{nd}$ mode of IL vibration is excluded because it is caused by the travelling wave group. As stated in Bourguet *et al.* (2011) that, when 0°<$\phi_{xy}$<180°, the trajectory of the cylinder motion is counter-clockwise, i.e. the cylinder moves upstream when approaching the CF vibration maxima. On the contrary, when 180°<$\phi_{xy}$<360°, the trajectory is clockwise. The switches between the counter-clockwise and the clockwise orbits usually match the anti-nodes of vibration.

Fig. 6 depicts the histograms of $\phi_{xy}$ evaluated from a complete vibration cycle representing the standing/travelling wave pattern. Fig. 6(a) presents the histograms of $\phi_{xy}$ within 19.5<*tU*/*D*<24 during which the lower part of the cylinder (*z*/*D* < 70) shows the standing wave pattern. In the lower part, $\phi_{xy}$ periodically varies along the span with several jumps of 360°. The wavelength of the variation is roughly 18*D*, except the one adjacent to the lower end. It can be observed that the transition from the counter-clockwise to the clockwise trajectory links with the anti-nodes of the CF vibration. While, the change from the clockwise to the counter-clockwise orbit relates with the nodes of the CF vibration and the anti-nodes of the IL vibration. Bourguet *et al.* (2011) stated that when 0°<$\phi_{xy}$<180°, energy-transfer was from fluid flow to structure vibration, and thus the large-amplitude vibrations were excited. However, when 180°<$\phi_{xy}$<360°, energy-transfer was reversed and the vibrations were damped out. This conclusion highly coincides with the present results. The upper part of the cylinder (*z*/*D* > 70) shows the combined standing and travelling wave pattern. The variation of the $\phi_{xy}$ is milder without jumps of 360°. Fig. 6(b) illustrates the histograms of $\phi_{xy}$ within 32.5<*tU*/*D*<40. No sharp transition from the counter-clockwise to the clockwise trajectory is found, which implies that the mid-span is dominate by the travelling wave vibration without obvious nodes and anti-nodes. It should be noticed that $\phi_{xy}$ shows invariant sections near the two ends (especially the upper one) indicating the local standing wave vibration.

### 3.5 Near-wake pattern

Fig. 7 shows the vortex-shedding patterns in the near-wake at two time instants. The vortices are visualized by using the iso-surfaces of $\lambda_2$ – the second eigenvalue of the symmetric tensor $\mathbf{S}^2 + \mathbf{\Omega}^2$, where $\mathbf{S}$ and $\mathbf{\Omega}$ are respectively the symmetric and antisymmetric parts of the velocity gradient tensor $\nabla \mathbf{u}$. The color on the iso-surfaces indicates of the vorticity in the spanwise direction. Fig. 7(a) shows the vortex-shedding pattern at *tU*/*D*=55 corresponding to the standing wave pattern. It is observed that the spanwise vortex structures are generally parallel to the cylinder indicating the prevalence of the interwoven vortex-shedding pattern. This is different to the vortex-

shedding pattern at $tU/D$ =66 as show in Fig. 7(b). At $tU/D$ =66, the separated vortex structures are oblique to the cylinder due to the predominant travelling wave vibration. Note that the vortex structures change their oblique directions if the propagation of the traveling wave flips over (the figure is not shown here).
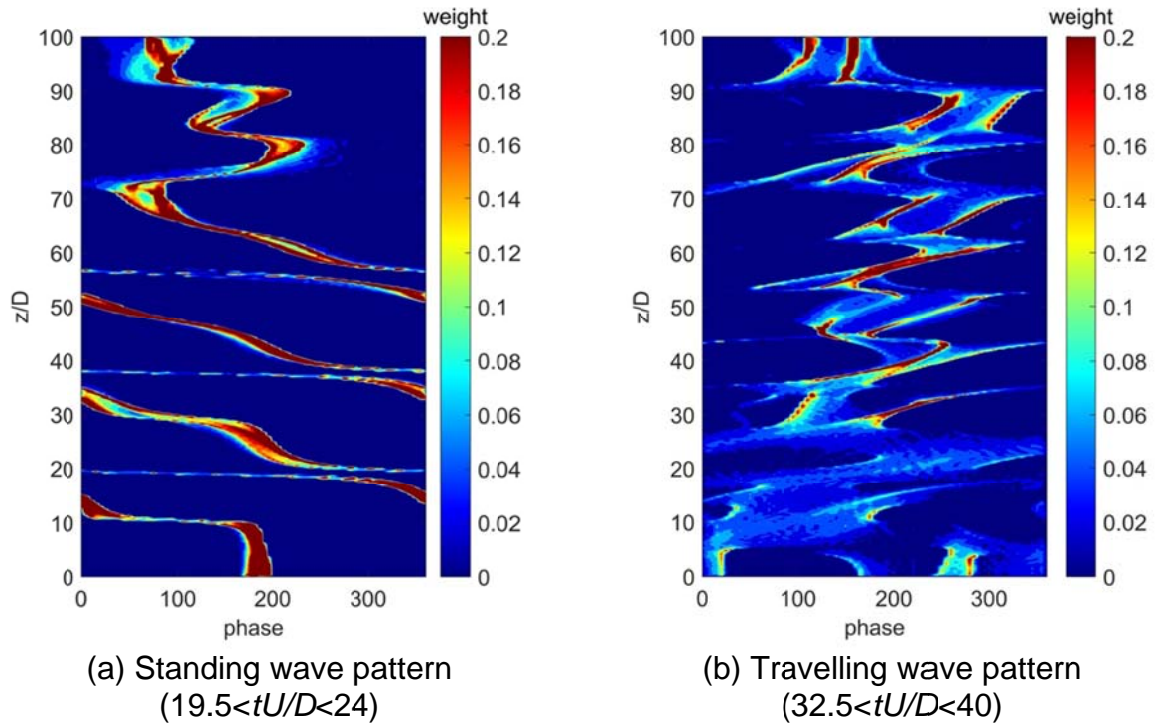


(a) Standing wave pattern
(19.5<$tU/D$<24)

(b) Travelling wave pattern
(32.5<$tU/D$<40)

Fig. 6 Histograms of the phase difference between the IL and the CF vibrations.

## 5. CONCLUSIONS

A numerical investigation on the vortex-induced vibration of an isolated cylinder in cross-flow is carried out. The immersed boundary method is applied to solve the interaction between the fluid and the flexible cylinder. The structural dynamics is simulated by using a 3D 2-node cable model. The slender cylinder, with an aspect ratio of 100, is top tensioned and pin-pin supported. The Reynolds number is 500, the normalized tension is 170, and the mass ratio is 4.2. A stretched Cartesian mesh with the smallest grid spacing $\Delta x = \Delta y = D / 32$ is adopted for space discretization in the *x-y* plane. A uniform mesh with a grid spacing of $\Delta z \approx 0.26D$ is used in the spanwise discretization. It is found that the IL and CF vibrations show the co-existence of multiple components. Mode competitions between the 10th and the 11th modes (IL) and between the 5th and 6th mode (CF) are observed. The 2nd mode with a very low vibration frequency dominates the IL vibration and its existence is attributed to the wave group propagating back and forth along the span. The time-space evolution of the displacement shows a scenario that the standing and travelling wave patterns alternately dominate the CF vibration. The spanwise distributions of the time-averaged and r.m.s. drag and lift coefficients are investigated. $C_{D,avg}$ and $C_{L,rms}$ show a variation similar to that of the CF displacement. While, $C_{D,rms}$ displays a distribution matching

the IL displacement's. Histograms of the *x-y* motion phase difference are evaluated from a complete vibration cycle representing the standing or travelling wave pattern. In the standing wave dominated vibration, the transition from the counter-clockwise to the clockwise orbit is connected with the CF vibration anti-node. While, the transition from the clockwise to the counter-clockwise trajectory is associated with the CF vibration node and the IL vibration anti-node. These switches are smoothed in the travelling wave governed vibration. Vortex structures behind the cylinder show the interwoven near-wake pattern when the standing wave pattern dominates, but the oblique near-wake pattern when the travelling wave pattern prevails.
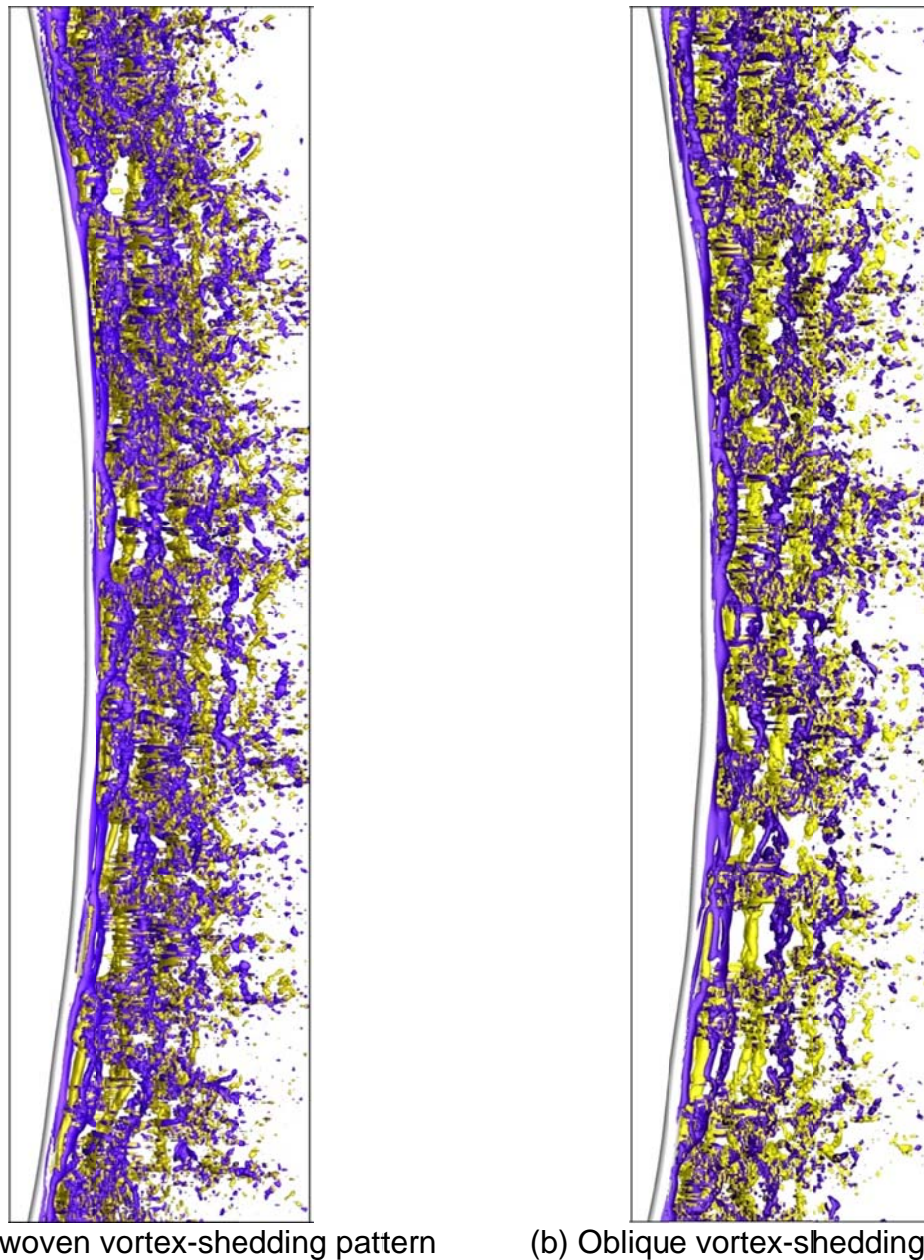


(a) Interwoven vortex-shedding pattern      (b) Oblique vortex-shedding pattern

Fig. 7 The vortex-shedding patterns in the near-wake.

## ACKNOWLEDGMENTS

## REFERENCES

Bourguet, R., Karniadakis, G.E. and Triantafyllou M.S. (2011), "Vortex-induced vibrations of a long flexible cylinder in shear flow", *Journal of Fluid Mechanics*, **677**, 342-382.

Brika, D. and Laneville, A. (1993), "Vortex-induced vibrations of a long flexible circular cylinder", *Journal of Fluid Mechanics*, **250**, 481-508.

Chaplin, J.R., Bearman, P.W., Huera-Huarte, F.J. and Pattenden, R.J. (2005), "Laboratory measurements of vortex-induced vibrations of a vertical tension riser in a stepped current", *Journal of Fluids and Structures*, **21**(1), 3-24.

Chen, W., Ji, C., Xu, W., Liu, S. and Campbell, J. (2015a), "Response and wake patterns of two side-by-side elastically supported circular cylinders in uniform laminar cross-flow", *Journal of Fluids and Structures*, **55**, 218-236.

Chen, W., Ji, C., Wang, R., Xu, D. and Campbell, J. (2015a), "Flow-induced vibrations of two side-by-side circular cylinders: Asymmetric vibration, symmetry hysteresis and near-wake patterns", *Ocean Engineering*, **110**, 244-257.

Huera-Huarte, F.J. and Bearman, P.W. (2009a), "Wake structures and vortex-induced vibrations of a long flexible cylinder - part 1: Dynamic response", *Journal of Fluids and Structures*, **25**(6), 969-990.

Huera-Huarte, F.J. and Bearman, P.W. (2009b), "Wake structures and vortex-induced vibrations of a long flexible cylinder - part 2: Drag coefficients and vortex modes", *Journal of Fluids and Structures*, **25**(6), 991-1006.

Ji. C., Munjiza, A. and Williams, J.J.R. (2012), "A novel iterative direct-forcing immersed boundary method and its finite volume applications", *Journal of Computational Physics*, **231**(4), 1797-1821.

Lucor, D., Mukundan, H. and Triantafyllou, M.S. (2006), "Riser modal identification in CFD and full-scale experiments", *Journal of Fluids and Structures*, **22**, 905-917.

Newman, D.J. and Karniadakis, G.E. (1997), "A direct numerical simulation study of flow past a freely vibrating cable", *Journal of Fluid Mechanics*, **344**, 95-136.

Peskin, C.S. (1972), "Flow patterns around heart valves: A numerical method", *Journal of Computational Physics*, **10**(2), 252-271.

Vandiver, J.K. (1993), "Dimensionless parameters important to the prediction of vortex-induced vibration of long, flexible cylinders in ocean currents", *Journal of Fluids and Structures*, **7**(5), 423-455.

Williamson, C.H.K. and Roshko, A. (1988), "Vortex formation in the wake of an oscillating cylinder", *Journal of Fluids and Structures*, **2**(4), 355-381.

Wu, X.D., Ge, F. and Hong, Y.S. (2012), "A review of recent studies on vortex-induced vibrations of long slender cylinders", *Journal of Fluids and Structures* **28**, 292-308.